INTERNATIONAL JOURNAL FOR NUMERICAL METHODS IN FLUIDS
Int. J. Numer. Meth. Fluids 2004; **46**:245–261 (DOI: 10.1002/fld.741)

A high-resolution scheme for low Mach number flows

Saugata Chakravorty and Joseph Mathew*,†

Department of Aerospace Engineering, Indian Institute of Science, Bangalore 560 012, India

SUMMARY

A method for computing low Mach number flows using high-resolution interpolation and difference formulas, within the framework of the Marker and Cell (MAC) scheme, is presented. This increases the range of wavenumbers that are properly resolved on a given grid so that a sufficiently accurate solution can be obtained without extensive grid refinement. Results using this scheme are presented for three problems. The first is the two-dimensional Taylor–Green flow which has a closed form solution. The second is the evolution of perturbations to constant-density, plane channel flow for which linear stability solutions are known. The third is the oscillatory instability of a variable density plane jet. In this case, unless the sharp density gradients are resolved, the calculations would breakdown. Under-resolved calculations gave solutions containing vortices which grew in place rather than being convected out. With the present scheme, regular oscillations of this instability were obtained and vortices were convected out regularly. Stable computations were possible over a wider range of sensitive parameters such as density ratio and co-flow velocity ratio. Copyright © 2004 John Wiley & Sons, Ltd.

KEY WORDS: compact schemes; low Mach number

1. INTRODUCTION

Compressibility effects can be neglected in low Mach number flows but density variations must still be accounted for when phenomena such as combustion are present. Then the time scale of acoustic waves is small compared to that of the hydrodynamic phenomena. An algorithm devised for general compressible flow will be expensive because time-steps must be small enough to resolve the acoustic waves while the integration period must remain large enough to capture the hydrodynamic phenomena. The chemistry time-scale must be dealt with separately. A suitable approximation which systematically removes acoustic waves without eliminating density variation is the low Mach number approximation proposed by Majda and Sethian [1]. The resulting problem can be solved by a small modification of the Marker and Cell (MAC) scheme [2] for incompressible flows. While applying this method to study an instability in low-density plane jets, we observed that calculations would break

*Correspondence to: Joseph Mathew, Department of Aerospace Engineering, Indian Institute of Science, Bangalore 560 012, India.
†E-mail: jmathew@alum.mit.edu

Published online 29 June 2004

Received 4 August 2003
Revised 21 April 2004

down where large density differences appeared at the edges of the jets. Rather than resorting to grid refinement to improve the resolution, we replaced explicit finite difference formulas with high-resolution compact ones. The improved resolution allowed larger density gradients to be computed without difficulty. In turn, this expanded the parameter space over which solutions could be obtained. The solutions showed qualitative differences as well because the details of evolution are dependent sensitively on resolution of fine scales. This paper presents this high-resolution scheme for the low Mach number equations and the improvements obtained. Of course, this approach is useful for the special cases of variable or constant density incompressible flows also.

The instability and transition of variable density jets results in growth of flow structures over a wide range of scales. So the special care taken for direct numerical simulations (DNS) needs to be brought to bear on these problems also. The primary difference is that DNS for turbulence is necessarily three-dimensional whereas the present stability problem is two-dimensional. Spectral methods are the natural choices because of their high efficiency: discretization error decreases exponentially as the grid is refined, phase errors are very small, and fast computations using FFTs are possible. However, being global functions, the classes of problems which can be solved are restricted to those in simple geometries whereas finite-difference (FD) methods are much more amenable to general geometries. An explicit FD approximation to a derivative depends on function values at neighbouring points and may be constructed to any desired degree of accuracy, but with increased stencil size. Another way of improving the accuracy of a finite-difference solution while retaining the advantage of applying arbitrary boundary conditions is to use the implicit FD methods which were made popular by Lele [3]. These methods are also called compact differences because the stencils are smaller than those for explicit methods of the same truncation error. Lele [3] showed that implicit approximations for derivatives, interpolation or filtering have higher resolving power: The numerical approximation remains close to the exact result for a larger range of scales compared to explicit formulas and thus recovers the advantages of spectral methods. These are also global methods and less flexible than schemes which use explicit difference formulas but do allow boundary conditions to be changed easily.

The order of accuracy, which is the order of the truncation error obtained from a Taylor series analysis of a numerical approximation, tells us how solutions can improve as the grid is refined. A higher-order scheme will deliver better solutions faster as the grid is refined. Either grid-refinement or increasing the order of the truncation error of the scheme when using the same grid can improve the accuracy with which a fixed scale is computed. Compact difference methods offer another way to improve the resolution of a fixed scale at the same truncation error and on the same grid. Coefficients of the truncation error of compact difference formulas are smaller as well. So such schemes are more efficient. This is especially important in DNS of transitional or turbulent flows because the grids employed are usually quite large and it is desirable to get the best solutions on a given grid rather than obtain convergence through a sequence of grid refinement. Lele's [3] analyses also showed that cell-centred formulas for derivatives offer better resolution of high wavenumber content than formulas based on grid values. Here we have used this idea to construct a high-resolution scheme.

There are two approaches to simulations of low Mach number flows. One way is to begin with the equations for compressible flow, devise a numerical scheme and then consider modifications to the numerical scheme when low Mach number flows are encountered. Typically some kind of pre-conditioning is done. A recent alternative proposal which is consistent in

time and therefore suitable for unsteady flows is by Sabanca *et al.* [4]. The other is to begin with the equations for low Mach number flows and adapt numerical schemes devised for incompressible flows to handle density variations. This second approach has been taken here. There have been several careful studies of methods to achieve high-resolution incompressible flow simulations. Morinishi *et al.* [5] showed how to construct higher-order finite difference schemes that remain fully conservative, so that such schemes can be used for DNS. Nicoud [6] has proposed the extension to solve the low Mach number equations. For variable density flows Bell and Marcus [7] had presented a method with a Godunov-type procedure to deal with sharp gradients and the generalization for high-resolution with adaptive gridding can be found in Reference [8]. The method presented here is distinct in that implicit difference formulas are being used to provide higher resolution at a given order.

In the following sections, the formulation of the method is presented and the performance of the method with respect to three unsteady flows are discussed. The first is the two-dimensional Taylor–Green problem which has an exact solution. It is useful for initial tests of the code. The second is the temporal evolution of eigenmodes of plane Poiseuille flow at constant density for both a growing and a decaying mode. The problem for the growing mode is especially sensitive because the eigenfunction has a rich structure near the channel walls, and its adequate resolution is essential to obtaining an accurate growth rate. The third is the oscillatory instability of a variable-density plane jet. In all cases the benefits of using the compact scheme are evident.

2. NUMERICAL SCHEME FOR LOW MACH NUMBER EQUATIONS

The governing equations for unsteady compressible flow are the Navier–Stokes equations. For low Mach number flow, it is well known that numerical integration of these equations is computationally demanding because of the severe restriction imposed on the time step by acoustic wave propagation which is much faster than flow speeds. Majda and Sethian [1] removed acoustic waves by expanding independent variables in powers of the Mach number. Density variations are still allowed. When the essential dynamics in flows such as low-speed combustion is dependent on density differences but not compressibility this procedure improves computational efficiency.

Let U_0, L_0, ρ_0 and T_0 be a reference velocity, length, density and temperature, respectively. The low Mach number equations were obtained [1] by expanding in powers of a small parameter $\varepsilon = \gamma M^2$, where $M = U_0/(\gamma R T_0)^{1/2}$ is the reference Mach number and γ is the specific heat ratio. At zeroth order (denoted by superscript 0), the equations for conservation of mass, momentum and energy are

$$\frac{\partial \rho^{(0)}}{\partial t} + \rho^{(0)} \frac{\partial u_i^{(0)}}{\partial x_i} + u_i^{(0)} \frac{\partial \rho^{(0)}}{\partial x_i} = 0 \tag{1}$$

$$\frac{\partial p^{(0)}}{\partial x_i} = 0 \tag{2}$$

$$\left(\frac{\partial \rho^{(0)} T^{(0)}}{\partial t} + \frac{\partial \rho^{(0)} u_j^{(0)} T^{(0)}}{\partial x_j} \right) = -(\gamma - 1) \frac{\partial p^{(0)} u_i^{(0)}}{\partial x_i} - \frac{\gamma}{Pr\, Re} \frac{\partial^2 T^{(0)}}{\partial x_i \partial x_i} \tag{3}$$

Here, velocity components u_i, lengths x_i, density ρ and temperature T have been scaled with the reference quantities mentioned above. Pressure p was non-dimensionalized with the reference thermodynamic pressure $\rho_0 RT_0$ and time t by L_0/U_0. Summation is implied on repeated indices. The two parameters are the Reynolds number $Re = \rho_0 U_0 L_0/\mu_0$ and the Prandtl number Pr. Also for an ideal gas, $p^{(0)} = \rho^{(0)} T^{(0)}$.

According to Equation (2) pressure is uniform in space to leading order. Equation (3) can be rewritten in the form of a constraint on the divergence of the velocity field

$$\frac{\partial u_i^{(0)}}{\partial x_i} = \frac{1}{\gamma p^{(0)}} \left[\frac{\gamma}{Pr\, Re} \frac{\partial^2 T^{(0)}}{\partial x_i \partial x_i} - \frac{\mathrm{d}\, p^{(0)}}{\mathrm{d}t} \right]$$

In closed systems, the pressure may change with time whereas it remains constant in open systems like free shear flows considered in this paper. Then $p^{(0)} \equiv 1$, and the constraint reduces to

$$\frac{\partial u_i^{(0)}}{\partial x_i} = \frac{1}{Pr\, Re} \frac{\partial^2 T^{(0)}}{\partial x_i \partial x_i} \tag{4}$$

To close the system of equations the first-order momentum equation is required.

$$\frac{\partial \rho^{(0)} u_i^{(0)}}{\partial t} + \frac{\partial \rho^{(0)} u_j^{(0)} u_i^{(0)}}{\partial x_j} = -\frac{\partial p^{(1)}}{\partial x_i} + \frac{1}{Re} \frac{\partial \tau_{ji}^{(0)}}{\partial x_j} \tag{5}$$

The deviatoric part of the stress tensor $\tau_{ij} = (\mu/\mu_0)(\partial u_i/\partial x_j + \partial u_j/\partial x_i)$ for a Newtonian fluid. Solutions were obtained by integrating the system of Equations (1) and (5) subject to constraint (4). Transport coefficients and specific heats were taken to be constants ($\mu = \mu_0$). Superscripts are omitted in the following discussions.

Incompressible flows are obtained when the velocity field is divergence free. Then, the right-hand side of Equation (4) is set equal to zero. Density variations in the field are still allowed, and the governing equations are (1), (4) and (5). For constant density flows, Equation (1) is also omitted.

2.1. Time stepping

The algorithm used here is similar to that used by McMurtry *et al.* [9] as an extension of the MAC scheme [2] for incompressible flows. The essential differences are in use of high-resolution formulas for spatial derivatives.

At each time step, first, the density was advanced by applying the second-order explicit Adams–Bashforth formula to Equation (1). Constraint (4) was used to evaluate the second term in Equation (1). Next, the pressure and velocity components were obtained in two steps. Equation (5) was split into the pair of equations

$$\rho^* u_i^* - \rho^n u_i^n = \Delta t \left[\frac{3}{2} (-A_i + D_i)^n - \frac{1}{2} (-A_i + D_i)^{n-1} \right] - \Delta t \frac{\partial p^n}{\partial x_i} \tag{6}$$

$$\frac{(\rho u_i)^{n+1} - (\rho u_i)^*}{\Delta t} = -\frac{1}{2} \frac{\partial \phi}{\partial x_i} \tag{7}$$

where $\phi = p^{n+1} - p^n$. Equation (6) is an explicit formula to determine $\rho^* u_i^*$. Convection and diffusion terms (A and D) were written according to the second-order Adams–Bashforth

formula while the pressure gradient terms were treated implicitly using second-order Crank–Nicholson formula. Equation (7) contains unknowns u_i^{n+1} and ϕ. On taking divergence of (7) (a discrete equivalent over cells is done in practice) and replacing $\partial(\rho u_i)^{n+1}/\partial x_i$ with the density derivative from Equation (1), we get a discrete equivalent of the following Poisson equation:

$$\frac{\partial^2 \phi}{\partial x_i \partial x_i} = \frac{2}{\Delta t}\left[\frac{\partial \rho^* u_i^*}{\partial x_i} + \frac{\partial \rho^{(n+1)}}{\partial t}\right] \tag{8}$$

Since the discrete gradient and divergence operations use second-order central differences the second derivative of ϕ is represented by the usual five-point stencil (in two dimensions) and $(\rho^* u_i^*)$ by two-point stencils in each direction. The density derivative source term in (8) was calculated using the second-order explicit backward difference formula

$$\frac{\partial \rho^{n+1}}{\partial t} = \frac{3\rho^{n+1} - 4\rho^n + \rho^{n-1}}{2\Delta t}$$

After the Poisson equation was solved, the velocity field u_i^{n+1} was obtained from Equation (7). A preconditioned conjugate gradient method was used to solve the Poisson equation. Symmetric successive over-relaxation was used as a preconditioner.

This procedure is known to be unstable for density variations larger than a factor of three. However, stable computations have been demonstrated (see, for example, Reference [10] or Reference [11]) at still larger ratios with a predictor–corrector approach which requires two computations of the Poisson problem per time-step. Such an approach would be necessary for treating realistic combustion problems, but has not been investigated here because the oscillating jet problem of our interest involves smaller density ratios.

2.2. High resolution spatial discretization

Here, as in the MAC scheme [2] for incompressible flows, the grids for velocity components u and v, and the pressure, are staggered with respect to each other. These grids form cells with pressure (density, temperature and any other scalars as well) located at the cell centre. Velocity components are defined at midpoints of faces whose normals are aligned with the respective component. Each component of the predictor step (6) is applied at the corresponding velocity component gridpoint to obtain the intermediate field. The Poisson equation (8) is constructed by taking divergence of Equation (7) numerically (or finding net mass flux into each cell).

In the MAC scheme [2] central differences are used for derivatives. The main differences in the scheme presented below are the procedures adopted to ensure that derivatives, and in turn the solutions, are calculated with better resolution. All derivatives of velocities or momenta per unit volume (ρu_i) were computed using the high-resolution compact difference formulas given below. The discrete form of the Poisson equation for ϕ (Equation (8)) was constructed from second-order explicit formulas for the divergence of the intermediate momentum ρu_i^* and gradient of ϕ. Although this appears inconsistent, it is common practice since it is known that the spatial order of accuracy of the velocity field is not affected by that of the pressure which serves to ensure the continuity constraint [12]. An explicit study which further demonstrates this insensitivity has been reported by Tafti [13]. In Section 3.1, we report a similar finding. Moreover, higher-order formulas for divergence violate an integrability constraint and can lead

to mass sources near boundary points so that the magnitude of the error in the solution can be larger even when the convergence rate is larger [13].

2.2.1. Implicit difference formulas. Lele [3] determined the resolving power of difference formulas with reference to the Fourier transform derivative which is an ideal method because this derivative is exact for all represented scales. If $\hat{f}(k) = \mathscr{F}[f(x)]$ is the Fourier transform of a function $f(x)$, the transform of the derivative $\mathscr{F}[\mathrm{d}f/\mathrm{d}x] = \mathrm{i}k\hat{f}(k)$, and the derivative can be recovered exactly by inverting $\mathrm{i}k\hat{f}(k)$. To compare the resolving power of a given difference formula, we substitute the Fourier series expansion $\Sigma\hat{f}(k)\exp(\mathrm{i}kx)$ into the difference formula and extract Fourier components of the derivative as $\mathrm{i}\tilde{k}(k)\hat{f}(k)$ where $\tilde{k}$ is an equivalent, or modified, wavenumber. The difference between $\tilde{k}$ and k is a measure of the error.

Let f_i denote values of f at gridpoints x_i $(i = 0, 1, 2, \ldots, N)$. Finite difference formulas for derivatives at gridpoints, f_i', are of the form $\sum_j \alpha_j f'_{i+j} = \sum_j \beta_j f_{i+j}$. Explicit formulas are obtained when coefficients $\alpha_j = 0$ for all $j \neq 0$. Otherwise, the formula is implicit. For these schemes, the modified wavenumber $\tilde{k} \approx k$ for low wavenumbers but then falls to zero at the highest represented wavenumber. So low wavenumber components are calculated accurately, whereas high wavenumber content is suppressed in the derivative. We select implicit difference formulas because they provide $\tilde{k} \approx k$ over a larger range of k for the same order.

For the Navier–Stokes equations applied on a staggered grid, several derivatives are required. Some derivatives are at the same locations where the variables are defined, while some are at offset locations. For the solutions presented here, high-resolution formulas which are at least fourth-order accurate at interior points were selected. Formulas were chosen such that sizes of the stencil of the unknowns (derivatives) and the stencil of the knowns (function values) were no more than three. Then, one formula is sufficient for all interior points. When the stencil is larger, it becomes necessary to use another formula near boundaries. A tridiagonal system has been solved in all cases. This requires only $O(N)$ operations.

The implicit fourth-order formula for the collocated first derivative used was ($\beta = b = c = 0$, $\alpha = \frac{1}{4}$ in formula (2.1.6) of Lele [3])

$$\frac{1}{4} f'_{i-1} + f'_i + \frac{1}{4} f'_{i+1} = 3\,\frac{f_{i+1} - f_{i-1}}{4h} \tag{9}$$

Cell-centred first derivatives were obtained from the fourth-order formula ($\beta = b = c = 0, \alpha = \frac{1}{22}$ in formula (B.1.1) of Lele [3])

$$\frac{1}{24} f'_{i-1} + \frac{11}{12} f'_i + \frac{1}{24} f'_{i+1} = \frac{f^*_{i+1/2} - f^*_{i-1/2}}{h} \tag{10}$$

Here $f^*_{i+1/2}$ is a function value at locations which are offset by half a grid interval. Where necessary such offset values were obtained by high-resolution interpolation using the sixth-order formula (corresponds to setting $\alpha = \frac{3}{10}, \beta = 0$ in formula (C.1.4) of Lele [3])

$$\frac{3}{10} f^*_{i-1/2} + f^*_{i+1/2} + \frac{3}{10} f^*_{i+3/2} = \frac{3}{4}(f_i + f_{i+1}) + \frac{1}{20}(f_{i-1} + f_{i+2}) \tag{11}$$

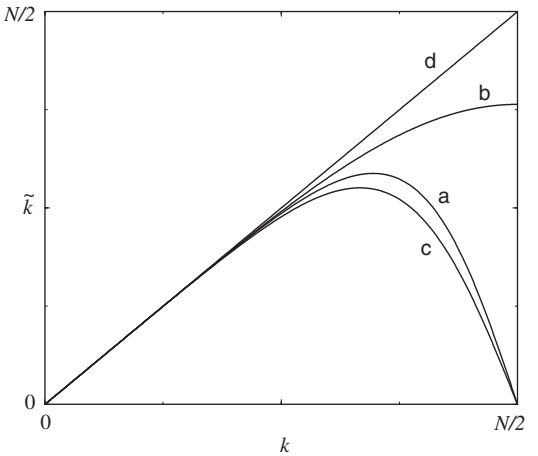

Figure 1. Effective resolution characteristics of first derivative approximations: (a) fourth-order, compact, cell-centred and interpolation $-\mathrm{i}D^*(k)I(k)$; (b) fourth-order, compact cell-centred; (c) fourth-order, compact difference; and (d) exact (Fourier).

Second derivatives, for viscous terms, were obtained from the fourth-order formula ($\beta = b = c = 0,\ \alpha = 1/10,\ a = 12/10$ in formula (2.2.6) of Lele [3])

$$\frac{1}{12} f''_{i-1} + \frac{10}{12} f''_i + \frac{1}{12} f''_{i+1} = \frac{f_{i-1} - 2f_i + f_{i+1}}{\Delta x^2} \tag{12}$$

These derivative and interpolation formulas, (10) and (11), can be written as relations between Fourier coefficients: $\hat{f}^*(k) = I(k)\hat{f}(k)$ and $\hat{f}'(k) = D^*(k)\hat{f}^*(k) = D^*(k)I(k)\hat{f}(k) = \mathrm{i}\tilde{k}\hat{f}(k)$. For exact operations (Fourier), interpolation $I(k) = 1$ and $D^*(k)I(k) = \mathrm{i}k$. Curve a in Figure 1 shows the effective resolution resulting from combining interpolation formula (11) with difference formula (10) the represented wavenumber range $0 < k < N/2$ when N is the number of intervals per period (taken as 2π here). Interpolation reduces the modified wavenumber of the cell-centred compact formula (curve b) at the high wavenumber end but remains slightly better than the standard fourth-order compact formula (curve c). Exact Fourier differentiation is the straight line $\tilde{k} = k$ (curve d). Resolution characteristics of formula (12) for the second derivative can be found in Reference [3].

The implicit formulas (10)–(12) are closed with end conditions. These are boundary equations which close the implicit formulas and not boundary conditions of the flow. For interpolation the boundary equation used was the implicit third-order formula $3f^*_{1/2} + f^*_{3/2} = f_0 + 3f_1$. Here, subscript 0 denotes a boundary location. For derivatives, we have used the third-order formula $11f'_1 + f'_2 = (-8f^*_{1/2} + 16f^*_{3/2} - 8f_1)/h$, generally, and the second-order formula $f'_1 = (f^*_{3/2} - f^*_{1/2})/h$ for derivatives of the cross term uv. For second derivatives, the boundary equation was the third-order explicit formula $f''_1 = (11f_0 - 20f_1 + 6f_2 + 4f_3 - f_4)/12h^2$.

The improved resolution offered by the compact differencing scheme leads to an increased possibility of aliasing error. Aliasing error becomes most prominent when the shorter length scales are marginally resolved and is dependent on aspects of the particular problem. One way to control aliasing error is to use filtering [3]. In the present simulations no explicit de-aliasing

algorithm has been used, but the discretization does provide for high wavenumber filtering (see Figure 1). It is known that discretizations of different forms of the advection terms result in different aliasing errors. In Equation (5), the convective terms are written in the conservative form $\partial(\rho u_j u_i)/\partial x_j$. Alternate forms are called the non-conservative form $\rho u_j \partial u_i/\partial x_j$, and the skew-symmetric form $\frac{1}{2}\,\partial \rho u_j u_i/\partial x_j + \frac{1}{2}\,\rho u_j \partial u_i/\partial x_j + \frac{1}{2}\,u_i \partial(\rho u_j)/\partial x_j$. For incompressible flow, aliasing error for the conservative and non-conservative forms are of opposite signs [14]. So the skew-symmetric form has been recommended to keep aliasing errors small. As a part of the present studies, the conservative, non-conservative and skew-symmetric forms have all been tested. Although there are differences between the solutions on a given grid, all forms converged to the 'correct' solutions as grids were refined.

3. NUMERICAL SOLUTIONS

Three problems are considered to assess different aspects of the proposed high-resolution method. The first is the Taylor–Green flow in two dimensions, which is an incompressible, doubly periodic flow with a simple closed form solution. The second is the linear instability stage of incompressible flow between parallel plates. This is a particularly sensitive test because the eigenfunction has a rich structure very close to the plates. To obtain even a qualitatively correct solution requires good resolution. The third case is the variable density plane jet flow which motivated this study.

3.1. Taylor–Green problem

The Taylor–Green flow is a doubly periodic array of two-dimensional vortices of alternating sense given by

$$u(x, y, t) = -\cos kx \sin ky \, \exp(-2k^2 t/Re)$$

$$v(x, y, t) = \sin kx \cos ky \, \exp(-2k^2 t/Re)$$

$$p(x, y, t) = -\tfrac{1}{4}(\cos 2kx + \cos 2ky) \, \exp(-4k^2 t/Re)$$

for any wavenumber k. The non-linear terms balance the pressure exactly. So there is only a viscous decay and no growth of harmonics. With the solution at $t = 0$ as the initial condition, solutions at subsequent times were found on a square of side 2π. Periodic boundary conditions were applied in both x and y directions. The present, compact difference scheme and the second-order, explicit difference scheme (MAC) were used.

Following Yang *et al.* [15] who took this flow to assess the performance of a convolution algorithm, we simulated at several Reynolds numbers $Re = 10^2, 10^4, 10^6$ and 10^{10} and wavenumbers $k = 1, 2$ and 5 on the same grid of 32×32 cells. The time step was $\Delta t = 0.001$. The L_∞ error of the u-component for a meaningful subset of these simulations ($Re = 10^2, 10^4$ and $k = 1, 5$) are listed in Table I. Also listed are data from Yang *et al.* [15] of their calculations with a Fourier pseudospectral method. At higher Re the solution changes little and the methods give nearly the same results. As is evident in the tables, the errors in the solutions with the compact scheme are about two orders of magnitude smaller than those with the

Table I. L_∞-error of velocity component u in numerical solutions of the two-dimensional Taylor–Green flow. The pseudospectral results are from Yang *et al.* [15].

k	Re	t	Psuedospectral	Second-order explicit	Fourth-order compact
1	10^2	1	$1.95E-10$	$6.26E-05$	$1.21E-07$
		10	$1.52E-10$	$5.23E-04$	$1.01E-06$
		20	$1.15E-10$	$8.57E-04$	$1.65E-06$
		30	$8.68E-11$	$1.05E-03$	$2.03E-06$
1	10^4	1	$7.91E-13$	$6.39E-07$	$1.23E-09$
		10	$7.59E-12$	$6.37E-06$	$1.23E-08$
		20	$1.48E-11$	$1.27E-05$	$2.46E-08$
		30	$2.23E-11$	$1.90E-05$	$3.68E-08$
5	10^2	1	$6.95E-08$	$2.39E-02$	$1.21E-03$
		10	$1.40E-10$	$3.19E-03$	$1.36E-04$
		20	$3.79E-12$	$5.32E-05$	$1.85E-06$
5	10^4	1	$1.18E-11$	$3.85E-04$	$1.98E-05$
		10	$1.38E-06$	$3.69E-03$	$1.89E-04$

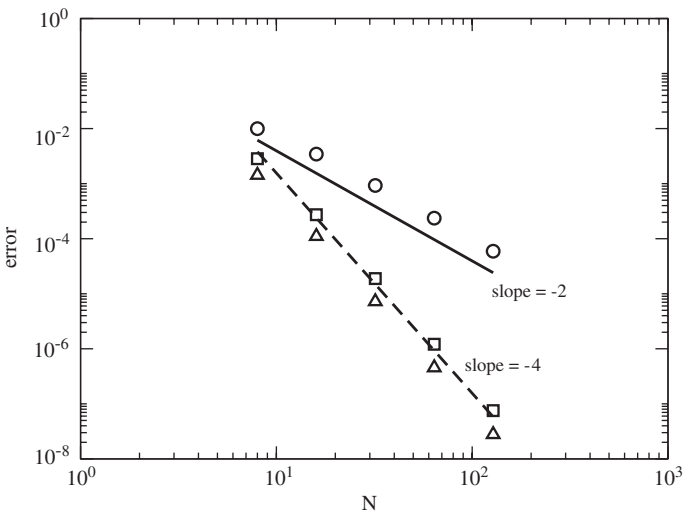

Figure 2. Convergence with grid refinement for different ways of calculating velocity derivatives. Divergence and pressure gradient constructed using the second-order central differences in all cases. ○: second-order central differences; □: fourth-order explicit formula; △: fourth-order implicit formula.

explicit scheme. The spectral method is certainly much better since the resolution is also much better.

Since this is a periodic flow, the spatial discretization formulas remain the same everywhere and convergence with grid refinement can be examined easily. Figure 2 shows the fall in L^∞ error of the u-component with grid refinement for three spatial discretization schemes.

Here $k = 1$, $Re = 100$ and the solutions are at $t = 1$. One is with second-order formulas for all derivatives (standard MAC scheme). The second has fourth-order explicit formulas for velocity derivatives of the momentum equations and the third has fourth-order compact differences. In all three cases, the divergence of the velocity field and the gradient of the pressure were constructed using the second order central difference formula. Figure 2 shows that the order of spatial accuracy follows that taken to discretize the velocity derivatives and that the magnitude of the error is smaller when compact differences are used.

3.2. *Temporal evolution of small disturbances on Poiseuille flow*

This is a demonstration of both resolving power and long-time accuracy. Standard linear stability analysis of Poiseuille flow provides eigenfunctions which can be added as a small perturbation to the base flow. The evolution of this perturbed flow obtained using a numerical scheme can be compared against the linear stability solution to assess properties of the numerical scheme. We consider both a decaying mode and a growing mode. The decaying mode is a mild test of resolution because the eigenfunction has a simple structure. Resolution error can cause a substantial departure for the growing mode because the eigenfunction has a rich structure near channel walls [16]. Even what may be considered reasonable grid clustering may not be adequate. Malik *et al.* [17], who had used Chebychev points, needed far more grid points compared to Rai and Moin [18] who had used a grid with spacing which grew as a geometric progression. Both had used finite-difference discretizations. So, this is a suitable test to demonstrate the benefits of using a high-resolution scheme.

According to linear stability analysis for Poiseuille flow [19], at a Reynolds number of 7500 based on channel width and centreline velocity, the eigenfunction for wavelength $\alpha = 1$ has a frequency $\omega_r = 0.24989154$ and growth rate of $\omega_i = 0.00223498$. Similarly, at $Re = 1000$, and unit wavelength, the frequency is $\omega_r = 0.34628486$ and growth rate is $\omega_i = -0.04212829$. A sequence of computations at constant density and at these two Reynolds numbers were carried out. The flow is periodic in the streamwise co-ordinate x and no-slip boundary conditions are applied at channel walls. The initial condition is the parabolic steady flow solution plus the relevant eigenfuction of small amplitude (about 0.1% of the steady flow centreline velocity).

Results of computing the decaying solution at $Re = 1000$ with three different schemes are shown in Figure 3. The standard MAC scheme (second-order explicit), a second scheme which used the fourth-order explicit difference formula for derivatives, and the present compact scheme (also of fourth order) were used. The grid had 16 points over one period along the channel and 16 points across. Clearly, the decay rate is closer to the exact value as the resolution of the scheme improves from second-order explicit to fourth-order explicit. The compact scheme provides a closer result. For completeness the solution using the compact scheme on a 32×32 grid is shown; it is essentially the same as the linear stability result. Note that the perturbation energy falls to quite small values but it is not contaminated by any kind of round-off error.

Figure 4 shows the evolution of perturbation energy for the growing mode at $Re = 7500$ for about eight time periods. All computations have 32 points per period along the channel. Solutions with the second-order explicit scheme are *qualitatively* wrong (energy falls) on the grids with 32 or 64 points across the channel. However, with 128 points, a positive growth rate is obtained. A similar result was obtained before [17]. With the fourth-order explicit method, the growth rate becomes positive when 64 points are used. The results with the compact

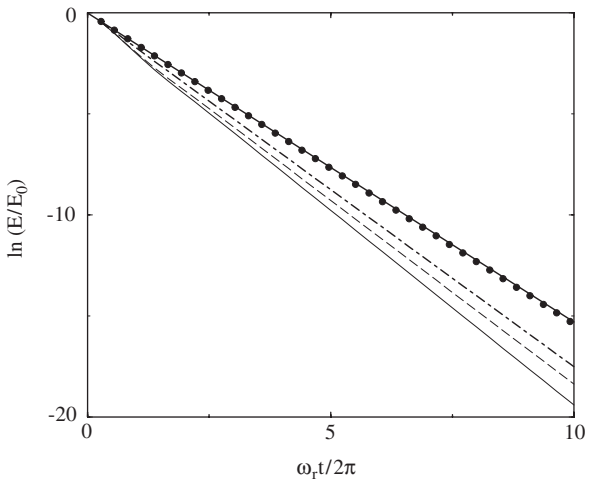

Figure 3. Evolution of energy of decaying mode of Poiseuille flow at $Re = 1000$. Effect on simulation of different schemes compared with Orr–Sommerfeld (exact) solution. All except one case obtained on 16×16 grid. —, second-order explicit differences; – – –, fourth-order explicit differences; — - —, compact scheme; •, compact scheme on 32×32 grid; —, exact.

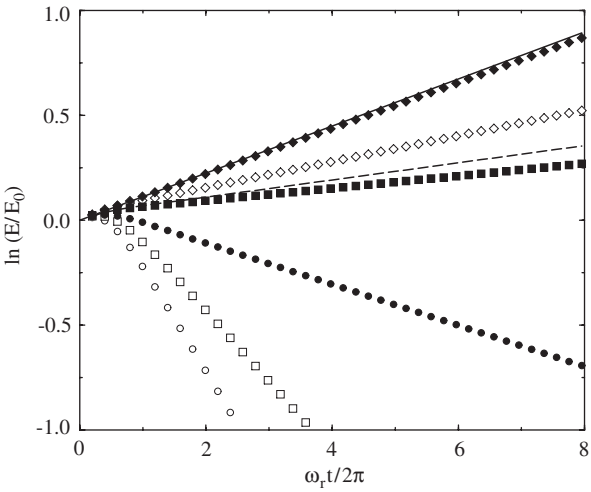

Figure 4. Growth of energy of growing mode of Poiseuille flow at $Re = 7500$. Effect on simulation of different schemes compared with Orr–Sommerfeld (exact) solution. —○—, second-order explicit 32×32 grid; —●—, second-order, 32×64; – – –, second-order, 32×128; —□–, fourth-order explicit 32×32; —■–, fourth-order, 32×64; —◇–, compact 32×32; —◆–, compact, 32×64; —, exact.

scheme illustrate the clear benefit of a high-resolution scheme. With 32 points itself, the solution is clearly better than even the fourth-order explicit scheme with 64 points. And with 64 points the solution is very nearly equal to the linear stability result. As can be expected,

the correct result can be obtained at the 32-point resolution itself when using a Chebyshev spectral method, since it has even better resolution characteristics [17].

All these solutions were obtained using the skew-symmetric form for the non-linear terms. The conservative form shows a growth rate which is smaller than the exact rate and converges from below as the grid is refined. The non-conservative form converges from above. Since the errors in the two are of opposite signs, but not equal in magnitude, the skew-symmetric form gives a closer result for a given grid but oscillates while approaching the exact result.

These two examples also emphasize the idea that the benefits of a high-resolution scheme will be realized only when solution structure has fine scales. In some cases, as in the decaying mode problem, grid refinement may be sufficient. In others, especially in three-dimensional computations, sufficient grid refinement may not even be possible. Further, although the higher-order explicit formula also provided some improvement in resolution, the compact scheme of the same order provided still further improvement and is, therefore, a more efficient scheme.

3.3. Unstable, variable-density, plane jet

The high-resolution method presented above was developed to study self-sustained oscillations of low density jets. It has been observed that oscillations appear in round jets when the ratio of jet to ambient fluid density drops below a critical value. It is observed in helium jets exhausting into air, heated jets, whether buoyant or not, and also plane jets (see Reference [20] for a plane jet experiment). The phenomenon is due to density variations rather than due to compressibility effects of high speed flows. Initial computations of plane jets using a standard method [9] reproduced self-sustained oscillations, but the flow fields seemed incorrect: jet-boundary shear layers rolled up into vortices but, as these vortices traveled downstream, they slowed down and grew considerably bigger. Wiggles appeared in some regions indicating loss of resolution. On comparing with solutions obtained with the high-resolution method, it appears that these are $O(1)$ errors which accumulate. So the improvement is important because it is not a small quantitative difference but is qualitative as well.

We consider symmetric solutions (seen in experiments [20]) of the plane jet flow which are determined by the velocity and density profiles at the inflow plane. The streamwise velocity component and density were

$$u(x=0,y)=\frac{1}{2}\left[\frac{1}{\lambda}+\tanh\left(\frac{2}{\delta_\omega}(y-y_0)\right)\right] \tag{13}$$

$$\rho(x=0,y)=\frac{1}{2}\left[\frac{1}{\lambda'}+\tanh\left(\frac{2}{\delta_\omega}(y-y_0)\right)\right] \tag{14}$$

The jet velocity at the centreline is U_j and velocity far from the jet when there is a co-flow is U_a. In Equation (13) $\lambda=(U_j-U_\mathrm{a})/(U_j+U_\mathrm{a})$ is a measure of the intensity of shearing, δ_ω is the shear layer vorticity thickness and the centre of the shear layer is at $y=y_0$. Similarly, in Equation (14), the density profile is characterized by the parameter $\lambda'=(R-1)/(R+1)$ where $R=\rho_j/\rho_\mathrm{a}$ is the jet to ambient fluid density ratio. No initial or inflow perturbations were imposed. Oscillations appeared spontaneously when the density ratio $R<0.9$, approximately, as in experiments. For a uniform density flow ($R=1$), perturbations at the inflow plane will cause the jet shear layers to roll up into vortices, but this instability disappears—vortices are convected out—when inflow perturbations are turned off.

A slip boundary condition was prescribed along the lateral planes to mimic freestream conditions. Prescribing outflow boundary conditions is always a sensitive issue in a spatially developing, unsteady flow. The boundary condition should be consistent with the physical processes of the flow. Since the outflow plane is a truncation of the jet, some error due to this truncation can be expected. The aim in such a situation would be to ensure that flow structures leaving the computational domain should do so with minimal distortion and without reflections travelling to every part of the computational domain. Here, the advective boundary condition,

$$\frac{\partial \rho u_i}{\partial t} + U_e \frac{\partial \rho u_i}{\partial x} = 0$$

was used along the outflow plane as in Reference [21]. Additionally, a correction was applied along the outflow plane to ensure overall mass balance [11]. Also, the location of the outflow boundary was progressively taken farther away and the frequency of oscillation was monitored.

With velocity difference across the jet shear layer as the velocity scale and vorticity thickness at inflow as the length scale ($\delta_\omega = 1$), simulations were conducted at Reynolds number $Re = 570$ and Prandtl number $Pr = 0.7$. The Reynolds number based on initial jet width $y_0 = 8$ is then $Re_{y_0} = 4560$.

The computational domain was a rectangle 120 units long in the streamwise direction and 40 units in the transverse direction on one side of the jet centreline. A uniform grid of 480×320 points gives a good solution with the present high-resolution scheme. On a coarse grid of 240×160 points, the lack of resolution shows up as wiggles. With the standard, second-order explicit scheme, even with a finer grid of 720×480 points the solution is not well-resolved everywhere.

On the coarse grid, computation time was roughly the same for both schemes. Most of the time was spent in the pressure solver which took slightly longer with the explicit scheme. Computation time increased slightly faster than linearly with grid refinement. CPU-time for the compact scheme on the medium grid is 4.2 times longer than on the coarse grid. With the explicit scheme the increase is 5.7 times. From medium to fine grid (explicit scheme) the increase is 2.5 times though the grid points increase only 2.25 times.

Figures 5(a) and (b) show density contours from simulations on the medium grid. The loss of resolution appears as wiggles in Figure 5(a). The rolled up vortex is also considerably larger and moves out slowly. Figures 6(a) and (b) show density distributions averaged over a few cycles of the oscillations. The difference in spreading is evident. The improved resolution also means that simulations are possible for a smaller density ratio. The density ratio could be as low as 0.5 without the calculations being unstable; the velocity ratio (U_j/U_a) could be as high as 40. In Figures 5 and 6 the jet to ambient velocity ratio is 39 and density ratio is 0.76.

To examine the convergence of these solutions with mesh refinement, magnitudes of the cosine transforms of the streamwise velocity component have been plotted in Figure 7. The velocity data was taken at $x = 90$ and at $t = 160$. The transforms were normalized so that the magnitude is unity at $k = 2$, and then for clarity, the curves were offset vertically by multiplying with suitable powers of 10. On the coarse grid (240×160) the spectra do not decay sufficiently fast at high wavenumbers with either scheme indicating that a larger wavenumber range is required. With the compact scheme and medium grid (480×320) a better fall off at high wavenumbers through several decades can be seen. With the second-order

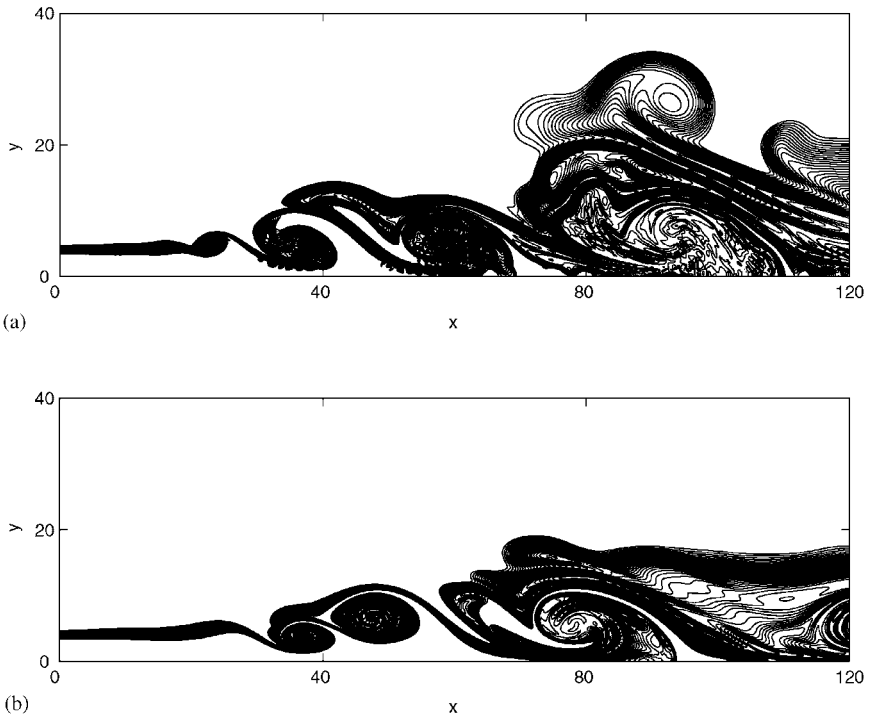

Figure 5. Density contours at an instant from simulation of unstable, variable density plane jet: (a) second-order explicit differencing; and (b) present scheme.

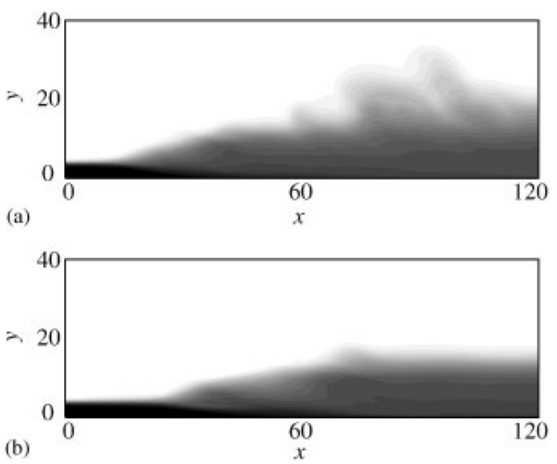

Figure 6. Time-averaged density contours from simulation of unstable, variable density plane jet: (a) second-order explicit differencing; and (b) present scheme.

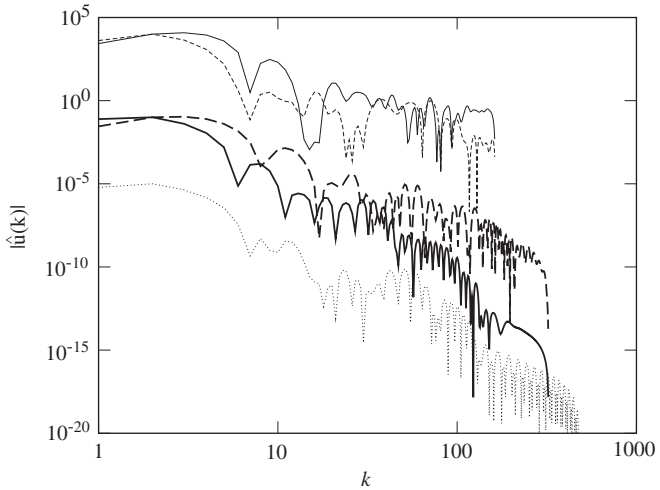

Figure 7. Magnitudes of cosine transform of streamwise velocity component at $x = 90$. Data have been normalized with the value at $k = 2$ and then multiplied by factors of 10 for clarity. ——, compact, coarse grid (240×160); —, compact, medium grid (480×320); – – –, second-order explicit, coarse grid; - - -, second-order explicit, medium grid; ·····, second-order explicit, fine grid (720×480).

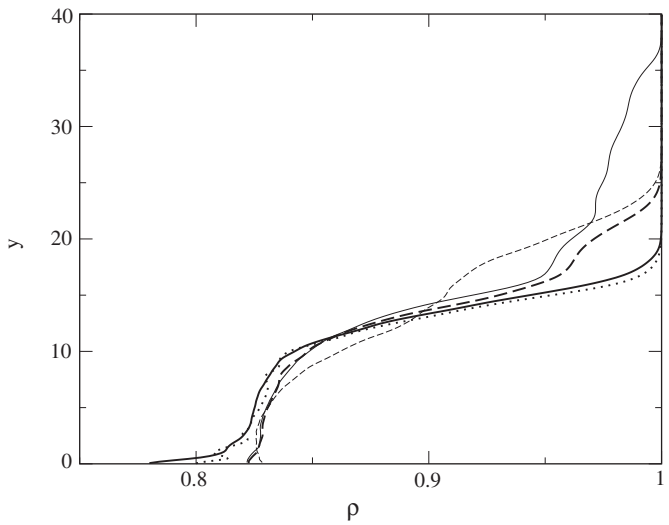

Figure 8. Mean density profiles at $x = 90$. ——, compact, coarse grid (240×160); —, compact, medium grid (480×320); – – –, second-order explicit, coarse grid; - - -, second-order explicit, medium grid; ·····, second-order explicit, fine grid (720×480).

scheme this fall off is seen only with the finer grid. But, once the solution is correctly resolved, the fall off with the second-order and compact schemes are similar. Note that these are from instantaneous profiles (which the method must resolve) and do not coincide. The effect

of under-resolution is not a mere clipping of a correct spectrum, but a wrong spectral distribution. In physical space this shows up as wiggles. The convergence of the mean flow can be seen in Figure 8. Mean density profiles at $x = 90$ taken from the same five computations have been plotted. Coarse grid solutions are not very different from the finer grid solutions over a part of the interface between light and heavy fluid. The differences are largely towards the outer edge of the jet (as can be inferred from Figures 5 and 6). These excursions at the outer edge disappear on the medium grid with the compact scheme and on the fine grid solution with the explicit scheme.

4. CONCLUSIONS

In this paper, some observations made in the course of developing an algorithm for low Mach number flow were presented. Spatial derivatives were obtained using implicit difference formulas which have better resolving power allowing a larger range of scales to be computed accurately. The test of channel flow linear instability clearly illustrates the beneficial effects of the high-resolution scheme. For the unstable, low density jet, the compact scheme was able to capture sharp density gradients without spurious oscillations. Solutions remained smooth and stable computations over a wider range of sensitive parameters such as density ratio and co-flow velocity ratio were obtained.

REFERENCES

1. Majda M, Sethian J. The derivation and numerical solution of the equations for zero Mach number combustion. *Combustion Science and Technology* 1985; **42**:185–205.
2. Harlow FH, Welch JE. Numerical calculation of three dependent viscous incompressible flow of fluid with free surface. *Physics of Fluids* 1965; **8**:2182–2189.
3. Lele SK. Compact finite difference schemes with spectral-like resolution. *Journal of Computational Physics* 1992; **103**:16–42.
4. Sabanca M, Brenner G, Alemdaroglu N. Improvements to compressible Euler methods for low-Mach number flows. *International Journal for Numerical Methods in Fluids* 2000; **34**:167–185.
5. Morinishi Y, Lund TS, Vasilyev OV, Moin P. Fully conservative higher order finite difference schemes for incompressible flow. *Journal of Computational Physics* 1998; **143**:90–124.
6. Nicoud F. Conservative high-order finite-difference schemes for low-Mach number flows. *Journal of Computational Physics* 2000; **158**:71–97.
7. Bell JB, Marcus DL. A second-order projection method for variable density flows. *Journal of Computational Physics* 1992; **101**:334–348.
8. Almgren AS, Bell JB, Colella P, Howell LH, Welcome ML. A conservative adaptive projection method for the variable density incompressible Navier–Stokes equations. *Journal of Computational Physics* 1998; **142**:1–46.
9. McMurtry PA, Jou WH, Riley JJ, Metcalfe RW. Direct numerical simulation of a reacting mixing layer with chemical heat release. *AIAA Journal* 1986; **24**(6):962–970.
10. Najm HN, Wyckoff PS, Knio OM. A semi-implicit numerical scheme for reacting flow. *Journal of Computational Physics* 1998; **143**:381–402.
11. Boersma BJ. Direct simulation of a jet diffusion flame. *Annual Research Briefs 1998*; Center for Turbulence Research, Stanford University, Stanford, 1998; 47–56.
12. Perot JB. An analysis of the fractional step method. *Journal of Computational Physics* 1993; **108**:51–58.
13. Tafti D. Comparison of some upwind-biased high-order formulations with a second-order central-difference scheme for time integrations of the incompressible Navier–Stokes equations. *Computer & Fluids* 1996; **25**: 647–665.
14. Kravchenko AG, Moin P. On the effect of numerical errors in large eddy simulations of turbulent flows. *Journal of Computational Physics* 1997; **131**:310–322.
15. Yang SY, Zhou YC, Wei GW. Comparison of the discrete singular convolution algorithm and the Fourier pseudospectral method for solving partial differential equations. *Computer Physics Communication* 2002; **143**:113–135.

16. Das A, Mathew J. Direct numerical simulation of turbulent spots. *Computer & Fluids* 2001; **30**:533–541.
17. Malik MR, Zang TA, Hussaini MY. A spectral collocation method for the Navier–Stokes equation. *Journal of Computational Physics* 1985; **61**:64–88.
18. Rai MM, Moin P. Direct simulations of turbulent flow using finite-difference schemes. *Journal of Computational Physics* 1991; **96**:15–53.
19. Orszag SA. Accurate solution of the Orr–Sommerfeld stability equation. *Journal of Fluid Mechanics* 1971; **50**:689–703.
20. Yu M, Monkewitz PA. Oscillations in the near field of a heated two-dimensional jet. *Journal of Fluid Mechanics* 1993; **255**:323–347.
21. Lowery PS, Reynolds WC. Numerical simulation of a spatially-developing, forced, plane mixing layer. *Report No. TF*-26. Department of Mechanical Engineering, Stanford University, Stanford, 1986.

